Acta Mechanica 149, 135–147 (2001)

ACTA MECHANICA
© Springer-Verlag 2001

Aerodynamic properties of a wing performing unsteady rotational motions at low Reynolds number

S. L. Lan and **M. Sun**, Beijing, China

(Received January 27, 2000)

Summary. The aerodynamic forces and flow structures of a wing of relatively small aspect ratio in some unsteady rotational motions at low Reynolds number (Re = 100) are studied by numerically solving the Navier-Stokes equations. These motions include a wing in constant-speed rotation after a fast start, wing accelerating and decelerating from one rotational speed to another, and wing rapidly pitching-up in constant speed rotation. When a wing performs a constant-speed rotation at small Reynolds number after started from rest at large angle of attack ($\alpha = 35°$), a large lift coefficient can be maintained. The mechanism for the large lift coefficient is that for a rotating wing: the variation of the relative velocity along the wing-span causes a pressure gradient and hence a spanwise flow which can prevent the dynamic stall vortex from shedding. When a wing is rapidly accelerating or decelerating from one rotational speed to another, or rapidly pitching-up during constant speed rotation, even if the aspect ratio of the wing is small and the flow Reynolds number is low, a large aerodynamic force can be obtained. During these rapid unsteady motions, new layers of strong vorticity are formed near the wing surfaces in very short time, resulting in a large time rate of change of the fluid impulse which is responsible for the generation of the large aerodynamic force.

1 Introduction

The flight mechanism of a small insect is gaining more attention than before due to possible applications in micromachines. Insects use their wings to provide lifting, propulsion and control forces for their flight. For these purposes the wings must frequently change direction, speed and orientation. Ellington [1] in a comprehensive review showed that conventional aerodynamic theory could not explain the generation of the required lift for insect flight and that an unsteady effect must play a major role in the force generation process. Since then, much work has been done for understanding the unsteady aerodynamics of insect flight (e.g., [2]–[5]).

Recently, Hamdani and Sun [6] studied the aerodynamic forces and flow structures of an airfoil performing some typical unsteady motions by numerically solving the Navier-Stokes equations (Re = 100). The motions were rapid acceleration and deceleration from one translation speed to another and rapidly pitching-up during translational motion. These motions were studied because some of them occurred during maneuvering flight, e.g., an insect might make fast turning by modulating the relative time of pitching-up of its two wings [7]. Moreover, even when insects were in normal forward or hovering flight, in order to provide both lifting and propulsion force, their wings must perform a flapping motion (alternating up-

strokes and downstrokes), which was a combination of the above simple motions. An analysis of the motions would provide the basis and insights for explaining the aerodynamics of the flapping motion. It was shown that in these fast unsteady motions very large aerodynamic forces were produced, and that the airfoil in small Reynolds number flow could produce a large aerodynamic force as effective as in large Reynolds number flow, or the effect of unsteady motion dominated the Reynolds number effect.

In the present study, we extend the above work to the case of a wing of relative small aspect ratio performing typical unsteady rotational motions. These motions include: wing in constant speed rotation after a fast start (similar to an insect wing in upstroke or downstroke motion, as sketched in Fig. 1), wing accelerating and decelerating from one rotational speed to another, and wing rapidly pitching-up during constant speed rotation. The wing considered in the present study is a rectangular wing with elliptical sections of 12 percent thickness. In most cases considered, the wing aspect-ratio is 2, and in some of the cases considered the aspect-ratio is 3.6 (for small insects, the wing aspect-ratio is between $2 \sim 3.5$).

2 The computational method

The Navier-Stokes equations for incompressible flow are numerically solved in the present study. For flow past a body in arbitrary motion, the governing equations can be cast in an inertial frame of reference using a general time-dependent coordinate transformation to account for the motion of the body. The inertial frame $(oxyz)$ is shown in Fig. 1. Also shown is a frame attached to the wing $(o'x'y'z')$, which is used in the grid-generation and in the description of the calculated results.

The Navier-Stokes equations are solved using the algorithm developed by Rogers et al. [8]. The algorithm is based on the method of artificial compressibility and uses a third-order flux-difference splitting technique for the convective terms and the second-order central difference for the viscous terms. Time accuracy in the numerical solutions is achieved by subiterating the equations in pseudotime for each physical time step.

At the inflow boundary, the velocity components are specified as freestream conditions while the pressure is extrapolated from the interior. At the outflow boundary, the pressure is set equal to the free-stream static pressure, and the velocity is extrapolated from the interior. On the wing surface, impermeable wall and no-slip boundary conditions were applied, and the pressure on the boundary is obtained through the normal component of the momentum equation.

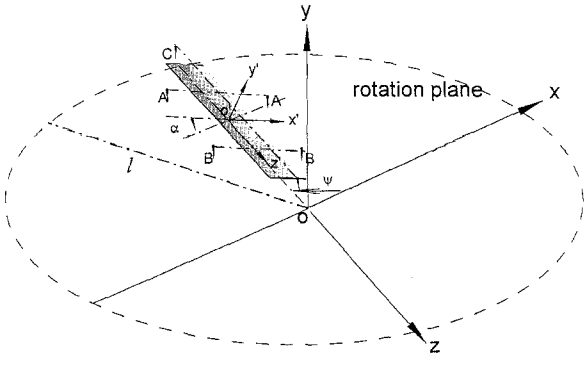

Fig. 1. A sketch of the wing and reference frames

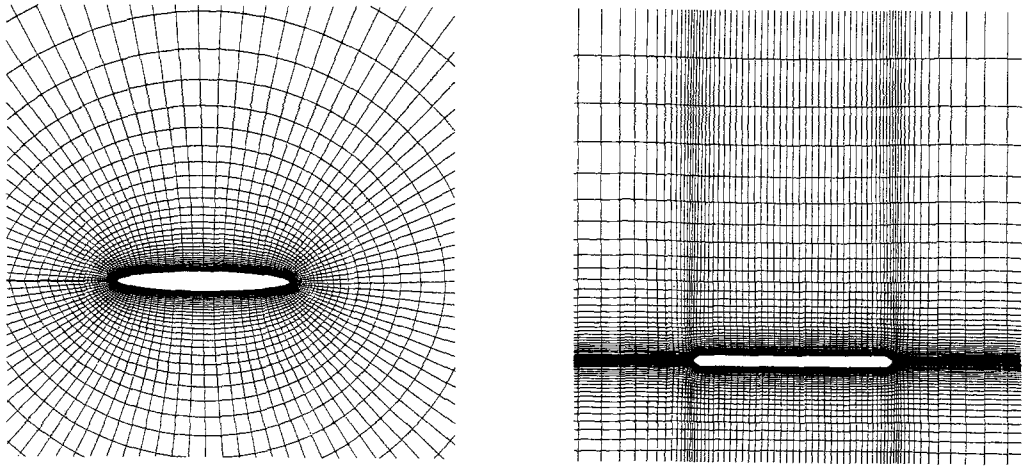

a b

Fig. 2. Mesh used for the wing

A body-fitted grid is generated by using a Poisson solver based on the work of Hilgenstock [9]. The grid topology used in this work was an O-H grid. Some portions of the grid used for the wing are shown in Fig. 2.

3 Results and discussion

3.1 Evaluation of solution accuracy

As with any numerical analysis, great care must be taken to insure the accuracy of the computed results. In order to verify the code, the flow around an elliptical airfoil of 6% thickness at zero angle of attack was calculated for Re = 10 ~ 1 000, and the drag coefficient was compared with the analytical solution of a flat plate [10], Fig. 3. The agreement with the analytical solution is very good. The code was also validated by measured pressure distributions on a wing at $\alpha = 11.8°$ and Re = 2×10^6 [11] (the turbulence model of Baldwin-Lomax was used

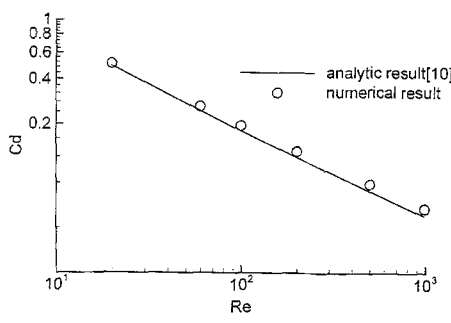

Fig. 3. Comparison between numerical calculation and analytical solution for the drag coefficients of a flat plate

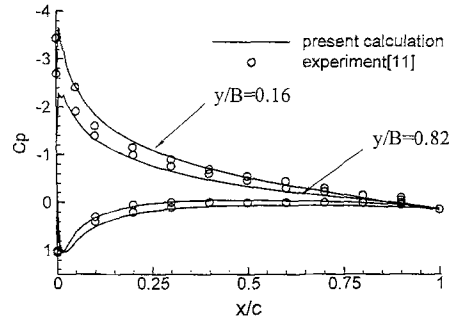

Fig. 4. Comparison between numerical calculation and experiment for surface pressure coefficients at two spanwise sections of a wing

in the calculation). A comparison between the computed and experimental results is shown in Fig. 4, and it is seen that they are in good agreement.

Grid sensitivity and the effect of the far-field boundary position were considered and will be discussed together with the calculated results in the next part of the paper.

3.2 Wing in constant-speed rotation after a fast start

The motion is sketched in Fig. 1, the wing rotates about the y-axis with constant speed after an initial acceleration motion from rest. This motion resembles that of an insect-wing in a upstroke or downstroke motion. In this paper, $\dot{\psi}$ denotes the rotational speed and $\dot{\psi}_0$ the constant rotational speed after the initial acceleration. In the initial acceleration, $\dot{\psi}$ is prescribed as

$$\dot{\psi}^+ = 0.5\dot{\psi}_0{}^+\left(1 - \cos\left(\pi t/\tau_a\right)\right), \qquad 0 \le \tau \le \tau_a\,. \tag{1}$$

In the above equation, $\dot{\psi}^+ = \dot{\psi}c/U, \dot{\psi}_0{}^+ = \dot{\psi}_0 c/U, \tau = tU/c$, where c is the chord length of the wing and U is a reference velocity, and τ_a is the time taken for accelerating the wing from rest to a rotational speed of $\dot{\psi}_0{}^+$. The reference velocity is taken as $U = r_0\dot{\psi}_0$, where r_0 is determined by $r_0 = \left(\int_A r^2 dA/A\right)^{1/2}$, where r is the radial distance and A is the wing area. For a rectangular wing, $r_0 = 0.64l$, where l is the length of the wing-span plus the distance between the wing-root to the rotational axis (Fig. 1). The Reynolds number is defined as $\mathrm{Re} = cU/\upsilon$ (υ is the kinematic viscosity) and is set equal to 100. Two cases of different wing aspect-ratio are considered in this section. The aspect-ratio is noted by λ. In the first case, $\lambda = 2$ and $l/c = 2.5$, and in the second case $\lambda = 3.6$ and $l/c = 4.5$. In the rotation, the angle of attack, α, of the wing is set equal to 35°. From our preliminary calculation, it was known that when α is between 30° and 60°, the lift is relatively large and does not vary significantly with α. Therefore 35° is considered in this study. In the calculation of this section, τ_a is set equal to 1.

Figure 5 gives the force and moment coefficients vs. τ for the case of $\lambda = 2$ (in this paper, C_L, C_d and C_m denote respectively the lift, drag and moment coefficients, and the moment is taken with respect to 0.25 chord location). In the figure, solid lines represent the results calcu-

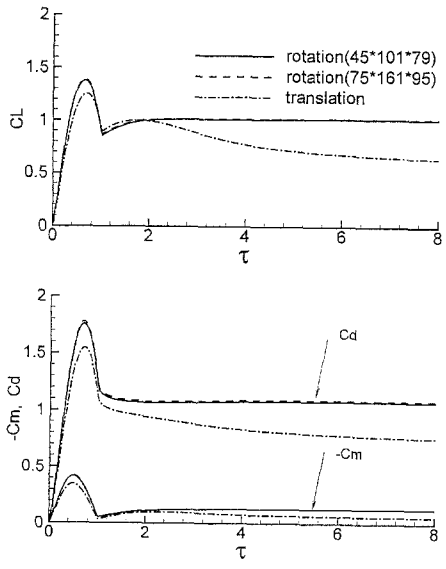

Fig. 5. Force and moment coefficients vs. τ, $\lambda = 2$

lated with a grid size of $45 \times 101 \times 79$, in the normal direction, around the wing section and in the spanwise direction, respectively (the distance between the first grid-line and the wing surface is $0.002c$). Dashed lines represent the results calculated using a grid size of $75 \times 161 \times 95$ (the distance between the first grid-line and the wing surface is $0.001c$). The outer boundary for both the two grids was set at 10 chord lengths away from the wing. It is seen that there is no difference between the results calculated using the two grids. The calculation was also conducted using a larger computational domain. In order to isolate the effect of domain size, the outer boundary was made farther away from the wing by adding more grid points in the normal direction to the first grid mentioned above. The calculated results showed that there was no need to put the outer boundary farther than 10 chord lengths from the wing. From the above discussion, it was concluded that the grid size of $45 \times 101 \times 79$ was proper for the present study.

It should be mentioned that at $\tau = 4$ the wing of $\lambda = 2$ has rotated about 120°, and at $\tau = 6$ the wing of $\lambda = 3.6$ would have rotated about 120°. The stroke angle of an insect wing is of the order of 120°. Therefore, the calculation in this section is carried out up to $\tau = 8$.

As can be seen in Fig. 5, in the acceleration phase ($\tau = 0 \sim 1$), a large force and a large moment appear (the behavior of the force and the moment during acceleration or deceleration will be discussed in detail in the next section). An interesting point in the results in Fig. 5 is that during the constant-speed rotation ($\tau > 1$) C_L reaches a value of about 1 in a short time and then keeps almost constant, and C_d and C_m behave similarly. For comparison, the calculation was done for the wing in translating motion at the same α. The speed at r_0 of the rotating wing was taken as the speed of the translating wing. The results are also included in Fig. 5 (dash-dot-lines). It is seen that in the constant speed phase of the translation ($\tau > 1$) C_L increases to a value of about 1 at $\tau \approx 2$ and then starts to decrease (decreasing to a value about 0.6 at $\tau = 8$). The above results show that the effect of wing rotation can keep the C_L at some large value.

The force exerted on a body moving in incompressible viscous fluid is related to the motion of vorticity around the body [12]. In order to explain the above behavior of the aerodynamic forces, contours of the spanwise component of the vorticity, ω_y, are plotted at two spanwise locations. These two spanwise locations, called "section A" and "section B" in this paper, are 25% and 75% of the wing-span from the wing root, respectively (Fig. 1). Figure 6 shows the vorticity plots for the wing in rotation. It is seen that from $\tau = 2$ to $\tau = 8$ the vorticity-plots do not vary with time, and the dynamic stall vortex on the upper surface of the wing does not shed, which explains why C_L and C_d do not vary with time during the constant-speed rotation. Figure 7 shows the velocity field in a spanwise plane (at 75% chord length from the leading edge). It is seen that there is a spanwise flow, and the direction of the flow is from the wing-root to the wing-tip. This spanwise flow might have stabilized the dynamic stall vortex and kept it from shedding. For a rotating wing, the suction pressure at the upper surface near the wing-tip where the relative velocity is high is stronger than that near the wing-root where the relative velocity is low. Therefore, there must be a pressure gradient in the spanwise direction, which is responsible for the spanwise flow mentioned above. Figure 8 gives pressure contours on the upper surface of the wing, showing that there is a pressure gradient directing from wing-root to the tip.

Figure 9 gives the vorticity contours in the symmetry plane of the wing in translation. It is seen that the vorticity on the upper surface of the wing moves downstream as time is increasing and is much more diffused than that of the rotating wing. The downstream motion of the vorticity is relatively fast between $\tau = 2$ and $\tau = 4$ and slower afterwards. This is consistent with the C_L variation during this time period (see Fig. 5). From the calculated velocity field of

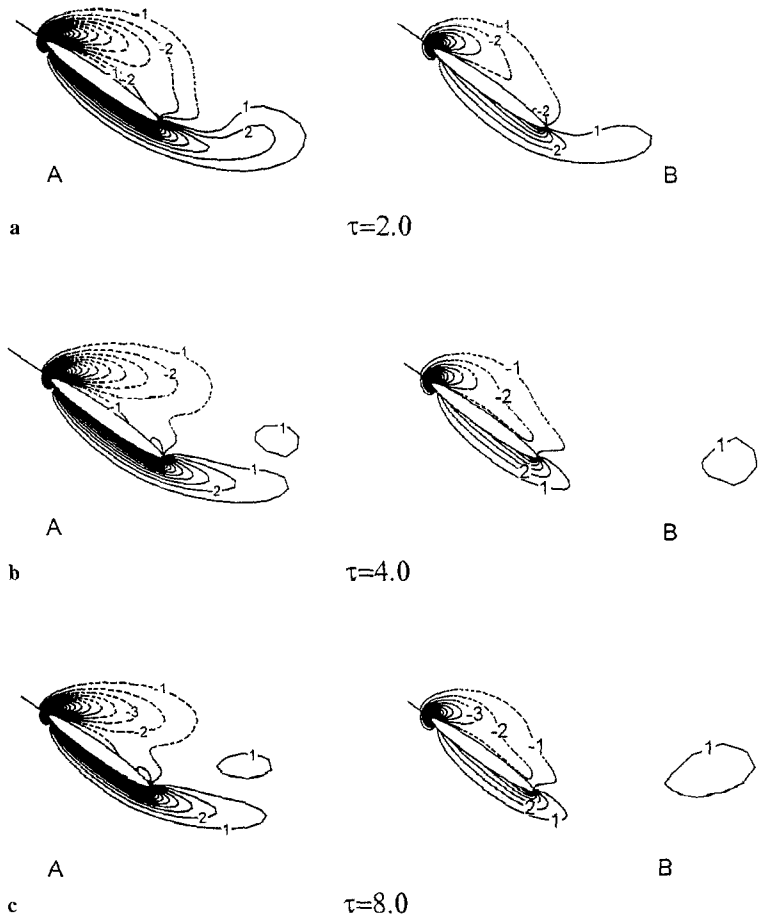

Fig. 6. Vorticity plots on section A – B of the wing in rotation, $\lambda = 2$

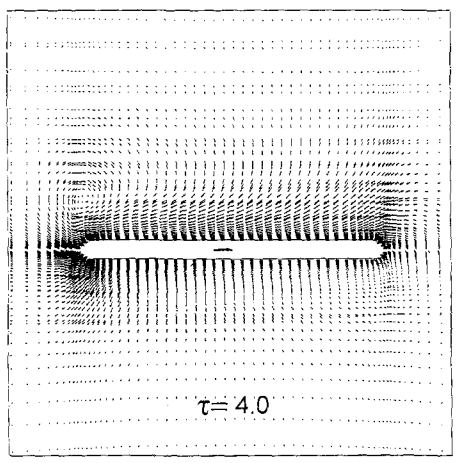

Fig. 7. Velocity field in a spanwise plane of the wing in rotation, $\lambda = 2$ (Arrow in wing represents the magnitude of reference velocity.)

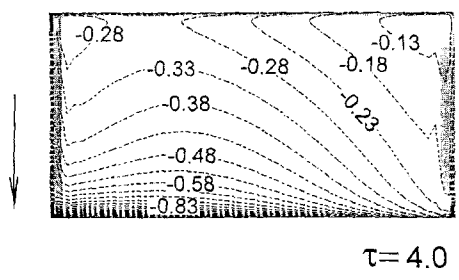

Fig. 8. Pressure contours on the upper surface of the wing in rotation, $\lambda = 2$ (Arrow shows the direction of wing rotation.)

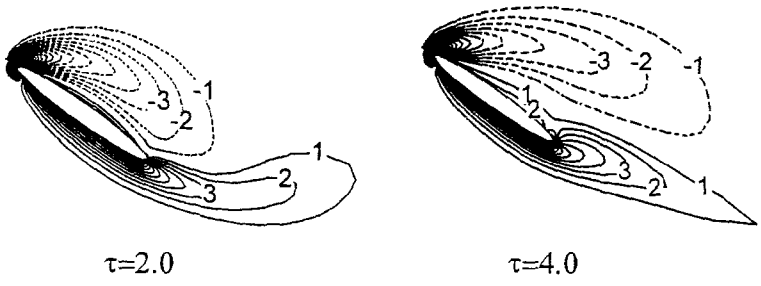

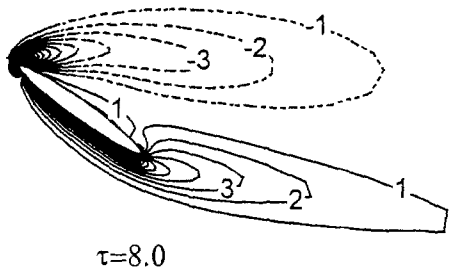

Fig. 9. Vorticity plots in the symmetry plane of the wing in translation, $\lambda = 2$

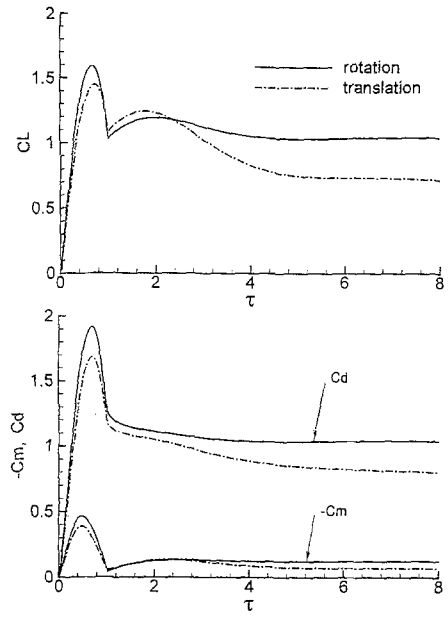

Fig. 10. Force and moment coefficients plots for the wing in rotation, $\lambda = 3.6$

the translating wing (not shown here), it was seen that there was no spanwise flow above the upper surface directing from wing-root to wing-tip like in the case of the rotating wing.

For the case of $\lambda = 3.6$, the force and moment coefficients vs. τ and vorticity plots are shown in Figs. 10–12. The qualitative behavior of the lift coefficient and its explanation by vorticity motion are similar to that of the case of $\lambda = 2$.

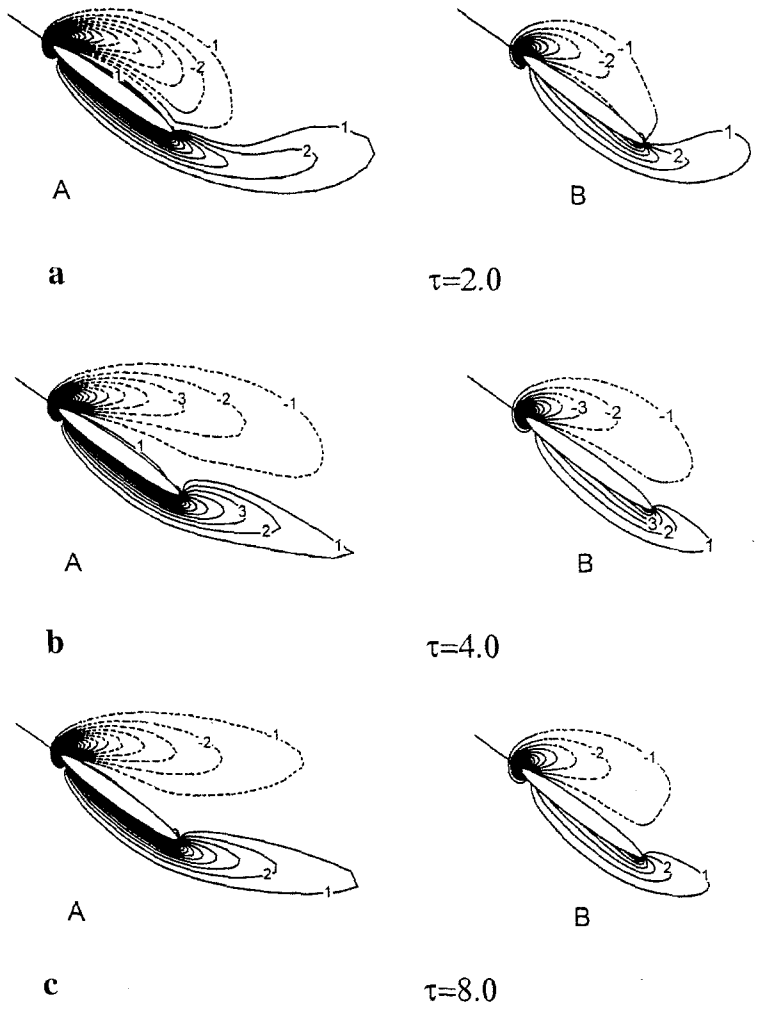

Fig. 11. Vorticity plots on the section A – B of the wing in rotation, $\lambda = 3.6$

3.3 Wing in rotational acceleration and deceleration

In this section, we consider the cases of a wing accelerating from rest to a constant rotational speed $\dot{\psi}_0{}^+$ and decelerating from constant speed rotation to rest. The aspect ratio of the wing is 2, and during the motions the angle of attack of the wing is 35°.

For acceleration from rest, $\dot{\psi}$ is given by Eq. (1), in which τ_a determines the acceleration. Three values of τ_a (0.5, 1 and 1.6), including the one used in the last section, are considered. The force and moment coefficients during the acceleration for $\tau_a = 1.0$ were already shown in Fig. 5 (between $\tau = 0$ and $\tau = 1$). Figure 13 gives the results for $\tau_a = 0.5$ and 1.6. From Fig. 5 and Fig. 13 it is seen that for the fast accelerating wing ($\tau_a = 0.5$) the variation of the force and moment coefficients with time closely follows that of the acceleration (their peaks almost coincide with that of the acceleration). When the acceleration becomes smaller ($\tau_a = 1.0, 1.6$), force and moment coefficients become smaller, and the variation with time becomes less similar to that of the acceleration (e.g., for the case of $\tau_a = 1.6$, the force and moment coefficients reach their peaks at about $\tau = 1.3$, much later than the acceleration with peak at $\tau = 0.8$).

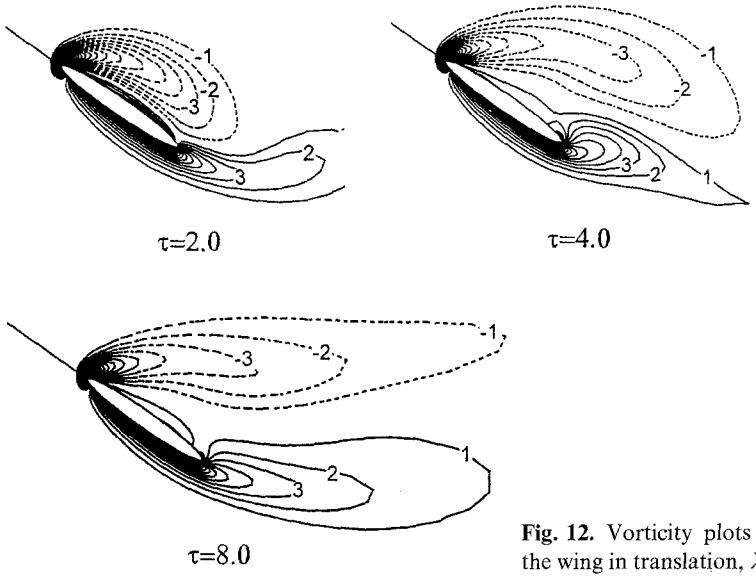

Fig. 12. Vorticity plots in the symmetry plane of the wing in translation, $\lambda = 3.6$

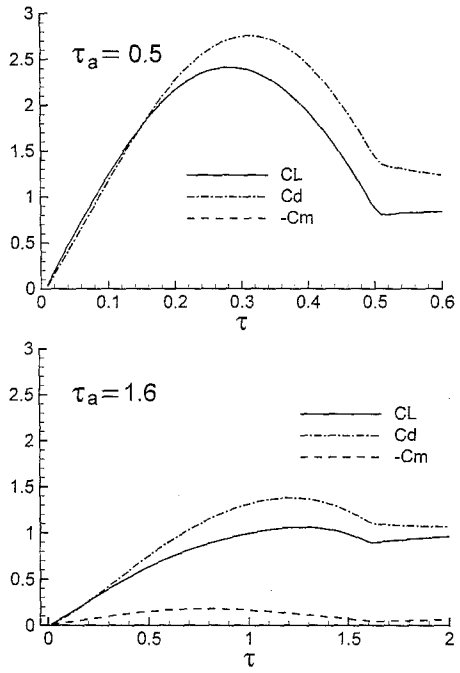

Fig. 13. Force and moment coefficients vs. τ during rotational acceleration

From Sect. 3.2, it was known that a short time after the wing was in constant speed rotation, the flow field (seen from the wing) stopped varying with time. Using this flow field as initial condition, the wing is decelerated from constant speed rotation to rest. The rotation velocity in the deceleration is given by

$$\dot{\psi}^{+} = 0.5\dot{\psi}_0{}^{+}\left(1 + \cos\left(\pi\tau/\tau_d\right)\right), \qquad 0 \leq \tau \leq \tau_d, \tag{2}$$

where τ_d is the time-duration of the deceleration. Figure 14 shows the force and moment coefficients vs. τ for $\tau_d = 0.5$ and 1.0. It is seen that the force coefficient behavior is approximately a mirror image of the acceleration case, C_L and C_d being negative.

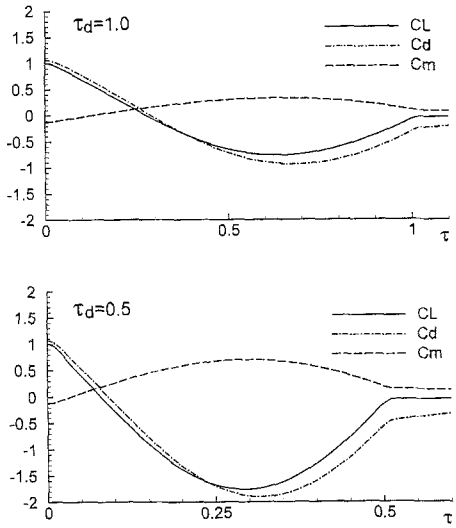

Fig. 14. Force and moment coefficients vs. τ during rotational deceleration

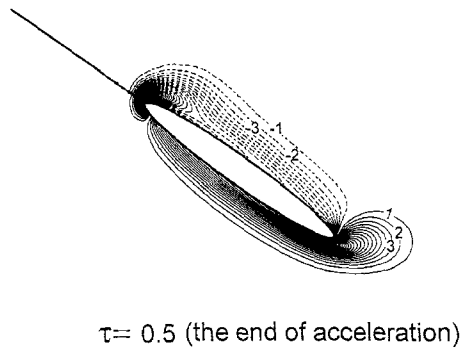

Fig. 15. Vorticity plots on section A at the end of the acceleration, $\lambda = 2, \tau_a = 0.5$

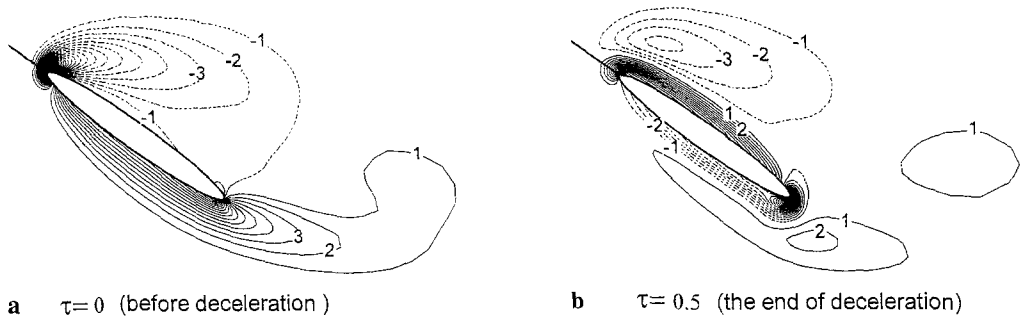

Fig. 16. Vorticity plots on section A during the deceleration, $\lambda = 2, \tau_d = 0.5$

The above results show that during fast acceleration and deceleration large aerodynamic forces and a large moment are produced, even if the aspect ratio is small and the flow Reynolds number (based on the constant speed after the acceleration or before the deceleration) is low. The reason for the large forces and the large moment is that large vorticity is generated in a short time by the wing during the fast acceleration or deceleration process, giving a large time rate of change of impulse to the fluid. Figures 15 and 16 give some samples of the vorticity plots for the cases of fast acceleration and deceleration, respectively. For the case of fast acceleration ($\tau_a = 0.5$), from the vorticity plot at the end of the acceleration (Fig. 15), it is seen that during the acceleration a negative vorticity layer forms around the leading edge and on the upper surface of the wing, and a positive vorticity layer forms on the lower surface, and part of it extends beyond the trailing edge to form the starting vortex. These vorticity layers are very strong and produced in a short time. For the case of fast deceleration ($\tau_d = 0.5$), from the vorticity-plot at the end of the deceleration, Fig. 16b, it is seen that during the deceleration new positive and negative vorticity-layers of large strength form on the upper and lower wing surfaces, respectively (under the previously existing vorticity regions). The formation of the new positive and negative vorticity layers is opposite to that of the acceleration

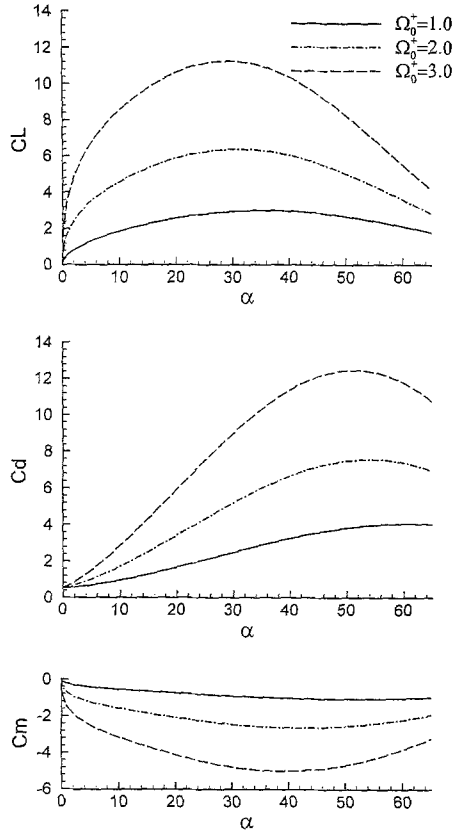

Fig. 17. Force and moment coefficients vs. α during the pitching-up, $\lambda = 2$

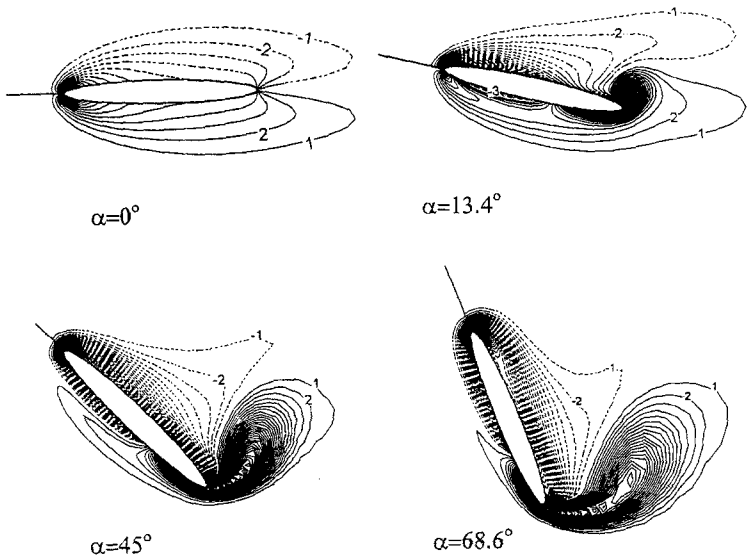

Fig. 18. Vorticity plots on section A at various α during the pitching-up, $\lambda = 2, \Omega_0{}^+ = 3.0$

case (compare Fig. 16b with Fig. 15). It is the interchanging of newly formed vorticity regions near the wing surface that causes the force and moment coefficients to behave in a reverse manner to that of the acceleration case.

3.4 Wing rapidly pitching during constant speed rotation

During constant speed rotation, the wing of $\lambda = 2$ is pitched up from $\alpha = 0°$ with angular velocity, Ω, given by

$$\Omega^+ = 0.5\Omega_0{}^+\left(1 - \cos\left(2\Omega_0{}^+\tau\right)\right), \tag{3}$$

where $\Omega^+ = \Omega c/U$; $\Omega_0{}^+$ represents the maximum value of Ω^+ (at $\tau = 0$ or $\alpha = 0$, Ω^+ is zero, at $\tau = \pi/2\Omega_0{}^+$ or $\alpha = \pi/4$, Ω^+ takes its maximum value, and at $\tau = \pi/\Omega_0{}^+$ or $\alpha = \pi/2$, Ω^+ becomes zero). The pitch-axis is at $0.25c$ from the leading edge of the wing. Three pitching rates, $\Omega_0{}^+ = 1, 2, 3$, are considered (according to Ref. [7], Ω^+ above 3 is common for small insects in their flight).

Figure 17 gives the force and moment coefficients vs. α. It is seen that even if the wing is of small aspect ratio and the Reynolds number is low, the aerodynamic forces are of very large values and the higher the pitching rate, the larger the force and moment coefficients. Before α is about 30°, C_L is much larger than C_d, and after α is about 45°, C_d becomes close to or larger than C_L. For the case of the highest pitching rate considered ($\Omega_0{}^+ = 3$), C_L is over 10 in a large range of α. Even for the case of a relatively small pitching rate considered ($\Omega_0{}^+ = 1$), C_L is over 2 in a large range of α. Based on our calculation, for a wing in constant-speed rotation at fixed α, C_L is not more than 1.2. Figure 18 gives vorticity plots at various angles α during the pitching motion for the case of $\Omega_0{}^+ = 3$. It is seen that before the pitching starts ($\alpha = 0$), very thick negative and positive vorticity layers exist around the wing. As the wing pitches up, new vorticity layers are generated, and a part of the newly generated positive vorticity layer at the lower surface of the wing moves downstream, forming the starting vortex. Since the pitching rate is high, the time taken for the generation and movement of the new vorticity is very short, resulting in a large time rate of change of the fluid impulse or large aerodynamic forces.

4 Conclusion

At a small Reynolds number (Re = 100), when a wing is performing constant-speed rotation after started from rest at a large angle of attack ($\alpha = 35°$), a large lift coefficient can be maintained. The mechanism for the large lift coefficient is that for a rotating wing the variation of the relative velocity along the wing-span causes a pressure gradient and hence a spanwise flow which can prevent the dynamic stall vortex from shedding. When a wing is rapidly accelerating or decelerating from one rotational speed to another, or rapidly pitching-up during constant-speed rotation, even if the aspect ratio of the wing is small and the flow Reynolds number is low, a large aerodynamic force can be obtained. During these rapid unsteady motions, new layers of strong vorticity are formed near the wing surfaces in very short time, resulting in a large time rate of change of the fluid impulse which is responsible for the generation of the large aerodynamic force.

Acknowledgements

This research was supported by the National Natural Science Foundation of China, Grant No. 19725210.

References

[1] Ellington, C. P.: The aerodynamics of hovering flight. III. Kinematics. Phil. Trans. R. Soc. London **305,** 41–78 (1981).
[2] Dickinson, M. H., Gotz, K. G.: Unsteady aerodynamic performance of model wings at low Reynolds numbers. J. Exp. Biology **174,** 45–64 (1993).
[3] Dickinson, M. H.: The effects of wing rotation on unsteady aerodynamic performance at low Reynolds numbers. J. Exp. Biology **192,** 179–206 (1994).
[4] Dickinson, M. H., Gotz, K. G.: The wake dynamics and flight forces of the fruit fly drosophila melanogaster. J. Exp. Biology **199,** 2085–2104 (1996).
[5] Liu, H., Ellington, C. P., Kawachi, K., Van den Berg, C., Willmott, A. P.: A computational fluid dynamic study of hawkmoth hovering. J. Exp. Biology **201,** 461–477 (1998).
[6] Hamdani, H., Sun, M.: Aerodynamic forces and flow structures of an airfoil in some unsteady motions at small Reynolds number. Acta Mech. (forthcoming).
[7] Dickinson, M. H., Lehmann, F. O., Gotz, K. G.: The active control of wing rotation by Drosophila. J. Exp. Biology **182,** 173–189 (1993).
[8] Rogers, S. E., Kwak, D., Kiris, C.: Numerical solution of the incompressible Navier-Stokes equations for steady-state and time-dependent problems. AIAA J. **29,** 603–610 (1991).
[9] Hilgenstock, A.: A fast method for the elliptic generation of three dimensional grids with full boundary control. Num. Grid Generation in CFM'88, pp. 137–146. Pineridge Press 1988.
[10] Schlichting, H.: Boundary layer theory, p. 148. McGraw-Hill 1979.
[11] Spivey, W. A., Moorhouse, G. G.: New insigths into the design of swept-tip rotor blades. Presented at the 26th Annual National Forum of the American Helicopter Society, Washington, D.C., June 1970.
[12] Wu, J. C.: Theory for aerodynamic force and moment in viscous flows. AIAA J. **19,** 432–441 (1981).

Authors' address: S. L. Lan and M. Sun, Institute of Fluid Mechanics, Beijing University of Aeronautics and Astronautics, Beijing 1000/83, P.R. China